CrystEngComm

Facile synthesis of PdSn alloy octopods through Stranski-Krastanov growth mechanism as electrocatalysts towards ethanol oxidation reaction

Journal:	*CrystEngComm*
Manuscript ID	CE-ART-02-2022-000242.R1
Article Type:	Paper
Date Submitted by the Author:	10-Mar-2022

Complete List of Authors:	Huang, Jingbo; Zhejiang University, Materials Science and Engineering Ji, Liang; Zhejiang Universit, Materials Scienci and Engineering Li, Xiao; Zhejiang University Wu, Xingqiao; Zhejiang University Qian, Ningkang; Zhejiang Universit, Materials Scienci and Engineering Li, Junjie; State Key Laboratory of Silicon Materials, Materials Science and Engineering Yan, Yucong; Zhejiang University, Department of Materials Science and Engineering Yang, Deren; Zhejiang University, School of Materials Science and Engneering Zhang, Hui; Zhejiang Universit, Materials Scienci and Engineering

PAPER

Facile synthesis of PdSn alloy octopods through Stranski-Krastanov growth mechanism as electrocatalysts towards ethanol oxidation reaction

Received 00th January 20xx,
Accepted 00th January 20xx

DOI: 10.1039/x0xx00000x

www.rsc.org/

Jingbo Huang,‡[a] Liang Ji,‡[a] Xiao Li,[a] Xingqiao Wu,[a] Ningkang Qian,[a] Junjie Li,[a] Yucong Yan,[a,c] Deren Yang[a] and Hui Zhang[a,b,*]

Pd-based nano-catalysts are critical to the commercialization of direct ethanol fuel cells (DFECs), however, the synthesis of Pd-based binary alloy nanocrystals with well-defined branches is still a great challenge. Here we report a facile seed-mediated approach for the synthesis of PdSn alloy octopods with precisely controlled branches and tunable compositions through Stranski-Krastanov growth mode. The PdSn octopod-like catalysts exhibited the prominently enhanced catalytic activity and stability towards ethanol oxidation reaction (EOR) with respect to commercial Pd/C in alkaline solution. Specifically, $Pd_{72}Sn_{28}$ octopods exhibited the highest mass and specific activity (2701 mA mg^{-1} and 11.27 mA cm^{-2}), which were 2.1 and 6.7 times higher than those of commercial Pd/C, respectively. Density functional theory (DFT) calculations reveal that the lowest d-band center of the (100) surface of $Pd_{72}Sn_{28}$ weakens the adsorption of the acetate-evolution key intermediate $*CH_3CO$, leading to the best catalytic activity towards EOR.

Introduction

As electrochemical energy conversion devices transforming chemical energy stored in ethanol to electric energy, direct ethanol fuel cells (DEFCs) have received great research interests and might play a critical role in energy sustainable use and carbon neutral.[1-3] However, the ethanol oxidation reaction (EOR) contains multiple steps, leading to sluggish reaction kinetics at the anodes of DEFCs, which impede the wide-spread commercialization of DEFCs.[4-6] Pd-based nanoparticles exhibit a comparable electrocatalytic activity towards EOR in alkaline media, however, their performance towards EOR still needs to be further enhanced.[7-11] Recently, tremendous efforts have been devoted to tune Pd-based nanocrystals,[12-13] one of them is to alloy Pd with a secondary component such as Ru,[14,15] Ag,[16,17] Cu,[18,19] Bi,[20,21] Sn,[22,23] Pb.[24] This secondary metal not only modifies the electronic structure of Pd and subsequently weakens the adsorption of poisonous species, but also brings a bifunctional mechanism.[6,7,20] The sites of the secondary metal with oxophilic capability can catalyze water to form the oxygenated species such as OH_{ads}, which substantially enhances the EOR properties by removing the CO-related intermediates on Pd sites.

Nanocatalysts with branched structures possess high specific surface area as well as low coordinated sites on the surface, thereby exhibiting pronounced enhancement in catalytic performance towards electrocatalysis.[25-27] For instance, Mu et al.[28] have reported the PtRuCu ternary alloy hexapods with greatly improved activity and durability towards methanol oxidation reaction (MOR) due to the unique dendritic structure. Recently, our group have developed an approach to the synthesis of PtPdCu ternary alloy hexapods, which showed excellent catalytic activities towards MOR thanks to low coordinated reaction sites at the corners and high specific surface area.[29] Stranski-Krastanov growth might represent a powerful approach to precisely control the number and distribution of branches in binary alloy nanodendrites. Stranski-Krastanov growth is typically carried out in sequence in two manners, firstly, atoms of the secondary component are deposited onto the surface of seeds layer-by-layer, later, after several layers of atoms are generated, it switches to the island growth mode.[30-34] The conversion of growth mode might be induced by the concentration of strain at some sites on the surface, or the accelerated deposition rate of secondary atoms.[30-32] If the subsequent island deposition of the secondary composition mainly takes place at the specific sites of the seeds, bimetallic nanocrystals with controlled branches will be generated. Recently, we have demonstrated that Pd@Pt core-shell hexapods and octopods were synthesized by the deposition of Pt atoms on Pd octahedral and cubic seeds based on the Stranski-Krastanov growth mechanism.[35] However, it is still a great challenge for the synthesis of Pd-based binary alloy nanoparticles with well-defined branches by a simple method.

Herein, we report a facile seed-mediated growth approach for the synthesis of PdSn alloy octopods with tunable compositions and

[a]State Key Laboratory of Silicon Materials and School of Materials Science and Engineering, Zhejiang University, Hangzhou, Zhejiang 310027, People's Republic of China. E-mail: msezhanghui@zju.edu.cn.
[b]Institute of Advanced Semiconductors, Hangzhou Innovation Center, Zhejiang University, Hangzhou, Zhejiang 310027, People's Republic of China.
[c]BTR New Material Group CO., LTD., GuangMing District, Shenzhen 518106, People's Republic of China.

‡ These authors contributed equally to this work.

the sizes of pods. Stranski-Krastanov deposition of Sn atoms onto the surface of Pd cubes and the interdiffusion of Pd and Sn atoms jointly promoted the formation of PdSn alloy octopods. The PdSn octopods with different compositions exhibited the substantially enhanced catalytic properties towards EOR relative to commercial Pd/C in alkaline solution. $Pd_{72}Sn_{28}$ octopods showed the highest mass and specific activities, which were 2.1 and 6.7 times higher than those of commercial Pd/C. Density functional theory (DFT) calculations indicated that the lowered d-band center of PdSn alloys weakened the adsorption of $*CH_3CO$ on the surface of the catalysts, and thus enhanced the catalytic performance.

Experimental section

Chemicals and materials

Sodium tetrachloropalladate (II) (Na_2PdCl_4, 99.99%), L-ascorbic acid (AA), potassium bromide (KBr), poly (vinylpyrrolidone) (PVP, MW ~ 55,000), tin (II) acetylacetonate ($C_{10}H_{14}O_4Sn$, or $Sn(acac)_2$, 99.9%), and 5% Nafion 117 solution were all purchased from Sigma-Aldrich. Oleylamine (OAm, 80%-90%) and tert-butylamine (99%) were purchased from Aladdin. Acetone, ethanol, toluene, cyclohexane, chloroform, and methanol were all purchased from Sinopharm Chemical Reagent Co., Ltd. (Shanghai, China). The commercial Pd/C (10 wt%) was purchased from Alfa Aesar. The resistivity of deionized (DI) water used in all the experiments was 18.2 MΩ·cm. All the chemicals and materials were used as received.

Synthesis of Pd cubes

The synthesis of Pd cubes was based on our previous report.[36] In a typical synthesis, 8.0 mL of DI water containing 105 mg of PVP, 60 mg of AA, and 500 mg of KBr was pre-heated to 80 °C under magnetic stirring for 10 min. Then, a 3.0 mL of DI water containing 57 mg Na_2PdCl_4 was quickly injected into the pre-heated solution, and was kept at 80 °C for another 3 h. The products were collected by centrifugation, washed three times with ethanol and acetone and then re-dispersed in ethanol for the phase transformation.

Phase transfer of Pd cubes

In a typical procedure, 5 mL of ethanol solution containing Pd cubes was mixed with 5 mL of OAm and 1 mL of toluene in a 20 mL glass vial, which was subsequently heated at 80 °C under magnetic stirring until the complete volatilization of ethanol. The Pd cubes in as-remained OAm solution was washed three times with a mixture of ethanol and cyclohexane, and then re-dispersed in OAm serving as the starting materials for the synthesis of PdSn octopods.

Synthesis of PdSn octopods

In a typical synthesis, 4 mL of OAm solution containing 1.9 mg of Pd cubes and 3 mg of $Sn(acac)_2$ was added to a 20 mL glass vial, and subsequently heated at 180 °C under magnetic stirring for 3 h. The product was collected by centrifugation, washed with a mixture of cyclohexane and ethanol for three times.

Characterizations

Transmission electron microscopy (TEM) images of the nanocrystals were taken through a Hitachi HT-7700 microscope operated at 100 kV. High-resolution transmission electron microscopy (HRTEM) images were taken through a FEI Tecnai F20 G2 microscope operated at 200 kV. Energy dispersive X-ray (EDX) analyses were performed on a FEI Titan ChemiSTEM equipped with a Super-X EDX detector system. The X-ray diffraction (XRD) patterns were performed on a Bruker D8 focus diffractometer in a scan range of 10-80°. Inductively coupled plasma atomic emission spectrometry (ICP-AES, IRIS Intrepid II XSP, TJA Co., USA) was used to determine the compositions of Pd and Sn in the samples. X-ray photoelectron spectrometer (XPS) analyses was taken on a scanning X-ray microprobe (Axis Supra, Kratos Inc.) with Al Kα radiation.

Preparation of carbon-supported catalysts

In a typical procedure, chloroform solution containing PdSn alloy nanocrystals with different compositions was added into another chloroform solution containing pre-dispersed carbon black nanoparticles (Vulcan XC-72R) under magnetic stirring. Then, the mixture was precipitated by centrifugation and re-dispersed in tert-butylamine and subsequently kept stirring for more than 72 h. Finally, as-prepared catalysts were centrifuged and washed five times with a mixture of methanol and DI-water.

Electrochemical measurements

All the electrochemical measurements were carried out in a standard three electrode cell system using an electrochemical workstation (CHI760E, Shanghai Chenhua Instrument Factory, China) at room temperature under atmosphere. A glass carbon rotating disk electrode (RDE, 0.196 cm^2) coated with catalysts was used as working electrode. A saturated calomel electrode (SCE) and a platinum wire were used as reference electrode and counter electrode, respectively. All the potentials were measured against the SCE and converted to reversible hydrogen electrode (RHE) according to E (vs. RHE) = E (vs. SCE) + 0.2438 V + 0.0592 × pH. 5 mg of catalysts was dispersed in 4 mL of DI water and 1 mL of isopropanol, added with 25 μL 5% Nafion 117 solution, and subsequently sonicated for 0.5 h to form a uniform ink. The mass of Pd loading on the RDE for all the catalysts was about 4 μg. Before electrochemical ethanol oxidation measurements, catalysts were pre-cleaned in Ar-saturated 1 M KOH through a cyclic voltammetry (CV) process between 0 and 1.2 V vs. RHE at a scan rate of 50 mV s^{-1} for dozens of cycles. The ethanol oxidation reaction (EOR) was conducted in a solution containing 1 M KOH and 1 M ethanol between 0.2 and 1.2 V vs. RHE at a scan rate of 50 mV s^{-1}. Mass and specific activities of all the catalysts were got from CV curves for EOR without IR compensation normalized to the mass of Pd and electrochemical active surface areas (ECSAs), respectively. The durability measurements were carried out under the same condition as EOR for an additional 500 cycles. As for CO stripping measurements, the catalysts-loaded RDE was firstly immerged in CO-bubbling 1 M KOH solution with a chronoamperometry test for 15 min to accomplish monolayer CO adsorption on the surface of nanocrystals. Then, the RDE was transferred into Ar-saturated 1 M KOH solution and carried with CV measurements between 0 and 1.2 V vs. RHE with a scan rate of 50 mV s^{-1} for 3 cycles. The ECSAs of all catalysts were calculated using the following equation:

$$\mathrm{ECSA} = \frac{Q_{\mathrm{CO}}}{0.42\ \mathrm{mC\ cm^{-2}} \times m_{\mathrm{Pd}}}$$

Where Q_{CO} was the charge by integrating the oxidation peak area of CO, m_{Pd} was the mass of Pd on the RDE, and 0.42 mC cm^{-2} was the charge required for the oxidation of monolayer CO.

Results and discussion

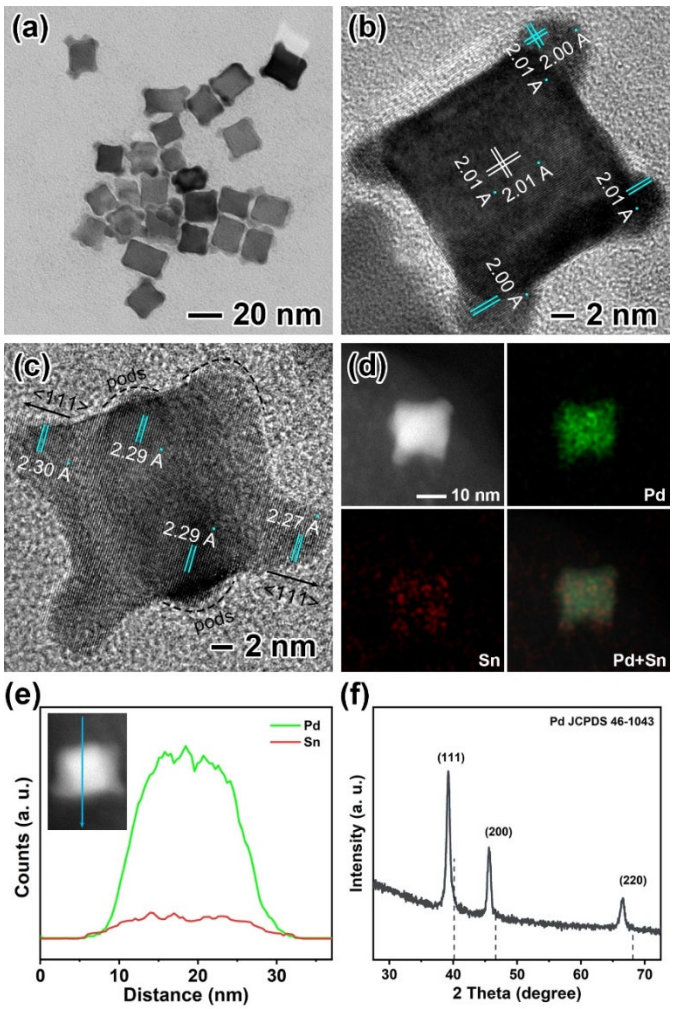

Figure 1. Morphological, structural, and compositional characterizations of the $Pd_{87}Sn_{13}$ octopods. (a) TEM image, (b, c) HRTEM images, (d) EDX-mapping image, (e) EDX line-scan profiles, and (f) XRD pattern.

The PdSn alloy octopods were synthesized by reduction of $Sn(acac)_2$ in OAm and the subsequent diffusion of Sn atoms into the lattice of Pd cubes based on our previous reported method.[16,37] Figure S1 shows morphological and structural characterizations of Pd cubic seeds. The lattice spacings of 1.95 Å in HRTEM image (Figure S1b) and no shift of peak positions in XRD pattern (Figure S1c) indicate that there is little strain in the lattice of Pd cubes. The size of cubes was measured to be 14.9 ± 1.2 nm (defined as distance face to face), as shown in Figure S1d. Figure 1 shows morphological, structural, and compositional characterizations of the PdSn octopods prepared by the standard procure. According to TEM images (Figure 1a and Figure S2a), most of nanocrystals show morphologies of cubes with pods stretching out at eight corners. Defined as distance face to face, the average size of octopods was measured to be 15.2 ± 1.7 nm (Figure S2b), suggesting a little volume increase relative to Pd cubic seeds due to the incorporation of Sn atoms. From HRTEM image of one octopod viewed along <100> direction (Figure 1b), lattices were measured to be 2.00~2.01 Å, either in the center of the cube or in the zone of pods, corresponding to {200} facets of PdSn alloys. Another octopod viewed along <110> direction is shown in Figure 1c, the fringes with a lattice spacing ranging from 2.27 to 2.30 Å can be indexed to the {111} facets of PdSn alloys. As can be seen, {111} facets are perpendicular to the longitudinal orientation of the pods, indicating the <111> preferential growth direction of pods. Both HRTEM images of octopods show well-resolved and continuous fringes in the same orientation from the central cubes to pods, suggesting that octopods are single crystals. EDX mapping images in Figure 1d reveal that Pd and Sn are distributed homogeneously throughout the octopods, confirming the formation of PdSn alloys. This demonstration is further supported by EDX line-scan analysis in Figure 1e. The XRD pattern in Figure 1f shows three most intensive peaks of face-centered cubic (*fcc*) structure, the positions of which shift to low angles relative to those of standard Pd, further proving the formation of *fcc*-structured PdSn alloys. From ICP-AES test, the atomic ratio of Pd to Sn is 87:13, labelled as $Pd_{87}Sn_{13}$.

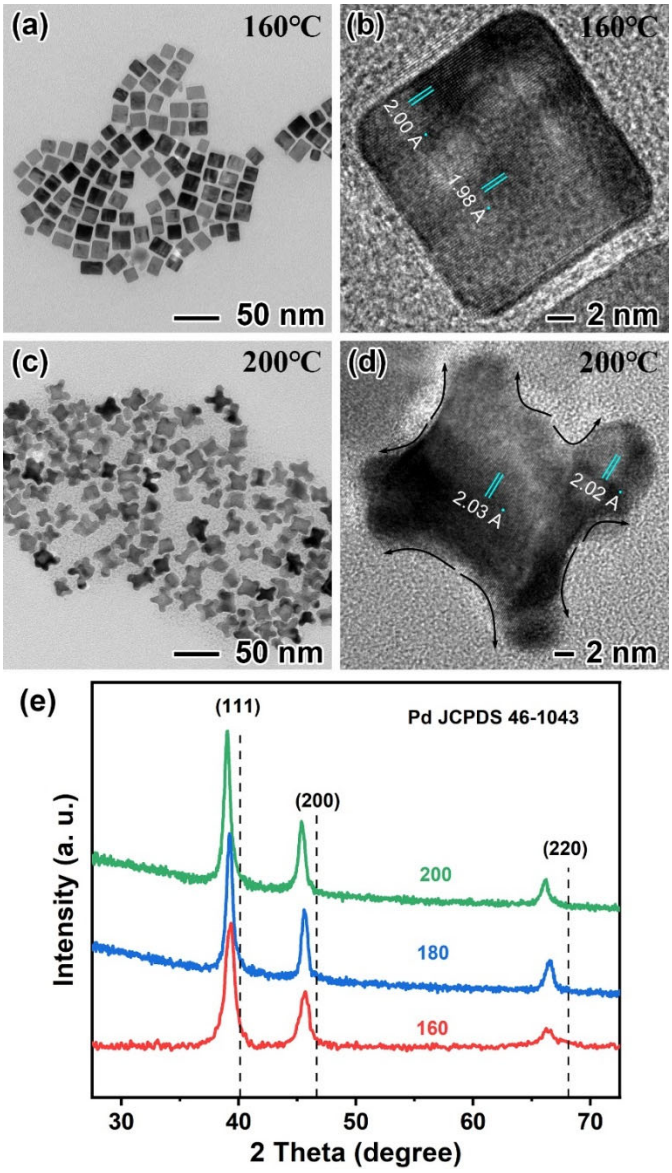

Figure 2. Temperature-dependent morphology and structure characterizations of the $Pd_{87}Sn_{13}$ octopods. (a, c) TEM images, (b, d) HRTEM images, and (e) XRD patterns at different temperatures: (a, b) 160 °C and (c, d) 200 °C.

The composition of octopods and the size of pods could be expediently tuned by varying the amounts of $Sn(acac)_2$ precursor in OAm while the quantity of Pd cubic seeds fixed. Figure S3 shows morphological, structural, and compositional characterizations of

the PdSn octopods prepared by the standard procure except decreasing the amounts of $Sn(acac)_2$ from 3 to 1 mg. From TEM image in Figure S3a, nanocrystals show cube-like shape with a little protrusion at some corners, and the size of cube is measured to be 15.2 ± 1.8 nm (Figure S3b). Two HRTEM images of the nanocubes viewed along <100> directions are shown in Figure S3, c and d. The lattice spacings of 1.97~1.99 Å are corresponding to {200} facets of PdSn alloys. TEM and HRTEM images show that the size of pods is remarkably smaller than that of octopods synthesized by standard procure. In addition, the size of pods is inhomogeneous at each corner of a cube. EDX mapping and line-scan analyses reveal that Pd and Sn distribute uniformly around the nanocrystals (Figure S3e, f). When increasing the amount of $Sn(acac)_2$ to 6 mg, the size of pods increases notably, as shown in Figure S4. The distance face-to-face is measured to be 14.6 ± 1.7 nm (Figure S4), a little smaller than the octopods prepared by the standard procedure. This result can be attributed to the interdiffusion between surface Pd atoms and Sn atoms at corners, together with the faster diffusion rate of surface atoms relative to the ones in the body.[38-40] HRTEM images of octopods viewed along <100> and <110> directions are shown in Figure S4c and S4d, respectively. Lattice spacings of 2.01~2.03 Å are corresponding to {200} facets and lattice spacings of 2.31~2.34 Å can be indexed to {111} facets of PdSn alloys. Pd and Sn are distributed approximately uniformly in the octopod according to EDX analysis (Figure S4e, f). The compositions of the aforementioned two PdSn alloy nanocrystals were characterized by ICP-AES and labelled as $Pd_{94}Sn_6$ and $Pd_{72}Sn_{28}$, respectively. XRD patterns of $Pd_{94}Sn_6$, $Pd_{87}Sn_{13}$, and $Pd_{72}Sn_{28}$ are shown in Figure S5. With the increase in the atomic ratio of Sn, the peak positions shift to low angle relative to pure Pd, on account of the lattice expansion of Pd with the incorporation of Sn atoms. As observed, each peak of $Pd_{94}Sn_6$ has a small broadened shoulder peak on the right (marked by red arrows), indicating the co-existence of the major PdSn alloy phase with another Pd-riched composition, suggesting the incomplete alloying of $Pd_{94}Sn_6$ octopods nanocrystals.

The PdSn alloy octopods were formed through the interdiffusion between Pd and Sn atoms, implying the key role of the reaction temperature.[41] Figure 2 shows the morphological and structural characterizations of PdSn alloy nanocrystals synthesized by the standard procure except for the different reaction temperature. When the temperature is 160 °C, nanocrystals show a cubic shape and no pod was generated at the corners of the cube (Figure 2a). Lattice spacings of as-synthesized cubes are measured to be 1.98-2.00 Å (Figure 2b), a little smaller than that of octopods obtained at 180 °C. As for nanocrystals formed at 200 °C, the length of the pods is prominently bigger and more irregular (Figure 2c). The {100} facets of the cubes become concave to some extent, so that it is hardly to recognize the shape of cubic seeds. From HRTEM image in Figure 2d, lattice spacings were measured to be 2.02-2.03 Å, indicating that the lattices expand gradually with the reaction temperature. This result is further demonstrated by XRD patterns in Figure 2e. The shift of peaks towards low-angle with the increase of the temperature suggests more Sn contents in the PdSn alloy nanocrystals.[42] The influence of temperature towards the product embodies two aspects, on the one hand, the rate and extent of the reduction and subsequent deposition of Sn atoms are significantly influenced by the temperature. As for PdSn cubes synthesized at 160 °C, temperature is not enough for the deposition of abundant Sn atoms onto Pd cubic seeds, leading to the difficulty in the formation of the pods at the corners. On the other hand, temperature has a great impact on the interdiffusion of Pd and Sn atoms. Pd atoms at the {100} facets of cubes move preferentially and rapidly towards as deposited Sn atoms at the eight corners at elevated temperature (see black arrows in Figure 2d), which causes the concave surfaces of nanocrystals.[38] As a contrast, the amount of $Sn(acac)_2$ can only influence the amount of as-deposited Sn atoms, thus having an impact on the size of pods and composition of nanocrystals. However, varying the amount of Sn atoms has nothing to do with the intrinsic diffusion coefficients of Pd and Sn atoms. Hence increasing the amount of $Sn(acac)_2$ will not bring the accelerated diffusion rate of surface Pd atoms towards corners, thus no concave surfaces appear.

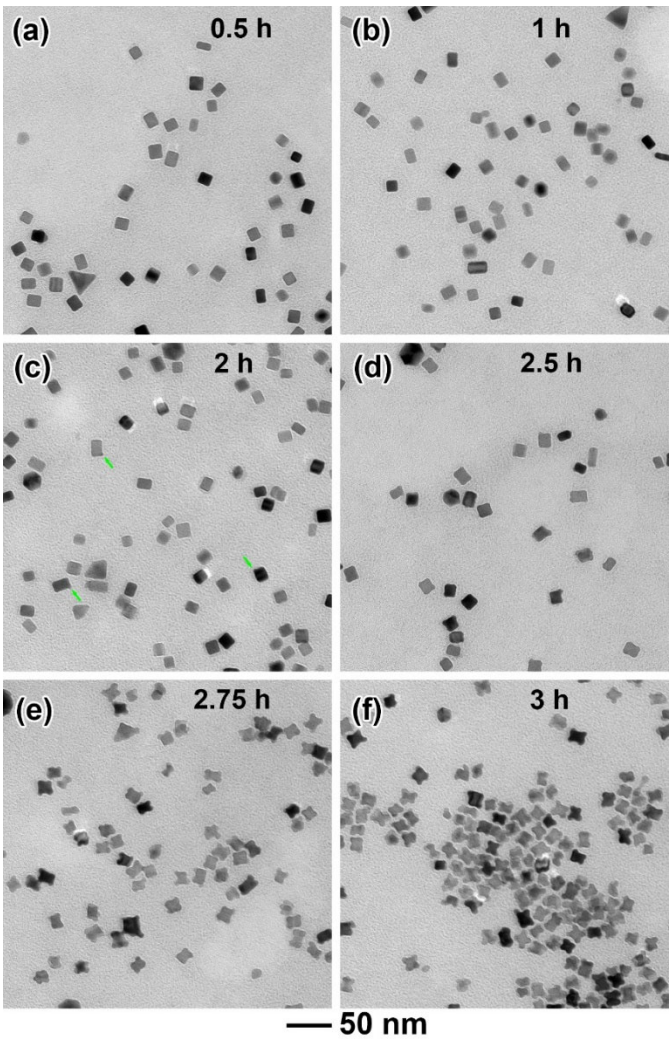

Figure 3. Time-dependent TEM images of the PdSn nanocrystals synthesized at 200 °C for different times: (a) 0.5, (b) 1, (c) 2, (d) 2.5, (e) 2.75, and (f) 3 h.

To understand the formation mechanism of PdSn alloy octopods, a series of samples taken from the reacting solution at different times were characterized. We chose octopods synthesized at 200 °C as the typical sample, since they have pods with the biggest size. At the initial stage from 30 min (Figure 3a) to 1 h (Figure 3b), nanocrystals remained the shape of cube. However, the lattice spacings of the nanocrystal at 1 h were measured to be 1.98-1.99 Å (Figure S6a), suggesting that Sn atoms have diffused into the lattice of Pd at this stage without breaking the morphology of cube. While the reaction was continued to 2 h (Figure 3c), most of the nanoparticles still kept the morphology of cube, however, small protrusions could be faintly observed at the corners of a few cubes (see arrows in Figure 3c). It is indicated that island growth begins to occur on a small portion of cubes at this time. From Figure 3d, most of nanocrystals started the

island growth mode before 2.5 h. From HRTEM image in Figure S6b, lattice spacings of 2.00-2.03 Å demonstrated the continuous incorporation of Sn atoms into the Pd lattice, and the shape of {100} facets was still observed. As the reaction time proceeded to 2.75 h (Figure 3e), the size of pods prominently got bigger, and the facets of {100} started to become concave, suggesting the rapid deposition of Sn atoms at corners as well as surface diffusion of Pd atoms from {100} facets towards pods at this stage. Finally, PdSn alloy octopods with concave {100} facets were generated at 3 h (Figure 3f), and the morphology of nanocrystals will not change even if the reaction was continued to 5 h (Figure S7). XRD patterns of the samples obtained at different reacting times are shown in Figure S8. With the proceed of reaction, the peak position of {111} facets shifted to low-angle gradually due to the continuous deposition and inwards diffusion of Sn atoms. After 2.5 h, the peak position varied rapidly relative to that before 2.5 h, indicating that the deposition rate of Sn had a dramatic increase starting from 2.5 h. Such behavior may induce the massive island deposition of Sn atoms at the corners of PdSn alloy cubes. The accelerated deposition rate of Sn atoms may be explained by LaMer mechanism of nucleation and growth that the concentration of Sn monomers surpassed one critical concentration at this stage and underwent a "deposition-burst" in solution.[43] In summary, at the initial stage of synthesis (before 2 h), Sn atoms were deposited onto the surface of Pd cubic seeds and diffused into the bodies at a slow speed with the shape of cube unchanged. Around 2 h, Sn atoms started to deposit preferentially to the corners of a small portion of nanocubes. With the reaction being continued, Sn atoms began to deposit at the corners of more and more cubes. Then, around 2.5 h, with the rapid increase of the deposition rate, plenty of Sn atoms were deposited to the corners and alloyed with Pd atoms moving from {100} facets, leading to the rapid growth of pods and the formation of concave facets of PdSn alloy octopods. The formation process is summarized by the schematic illustration in Figure 4.

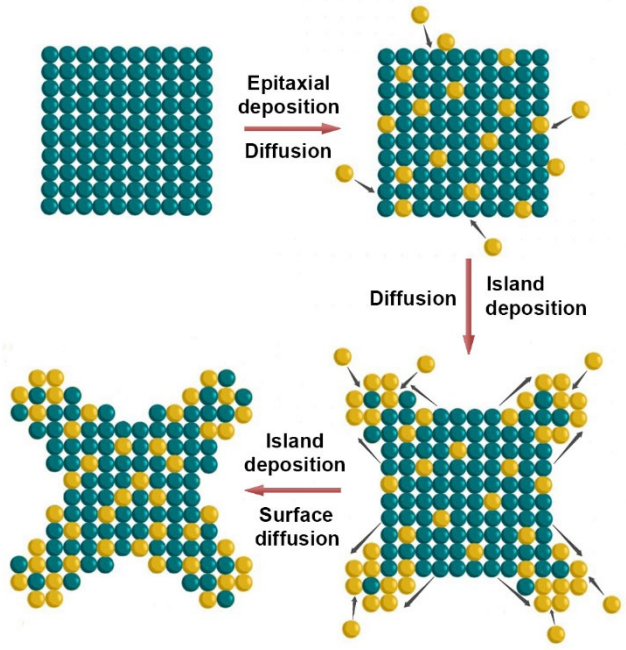

Figure 4. Schematic illustration showing the formation process of the PdSn octopods synthesized at 200 °C through the S-K growth mode. The cyan and yellow balls are corresponding to Pd and Sn atoms, respectively.

To explore the extensibility of this synthetic approach, we synthesized PdSn nanocrystals using Pd cubes with the sizes of 6 nm and 10 nm as seeds, as shown in Figure S9. For PdSn nanocrystals using 6 nm Pd cubes as seeds, the morphology of the nanocrystals got round without the formation of pods (Figure S9b). On the one hand, the corners of 6 nm Pd cubes are not so sharp-edged as corners of 15 nm Pd cubes, which is against the deposition of Sn atoms to the corners. On the other hand, the interdiffusion of 6 nm Pd cubes and Sn atoms is dominant by the surface interdiffusion due to the small size of seeds, leading to the formation of nanoparticles with round surface. Using 10 nm Pd cubes as seeds, PdSn octopods nanocrystals were synthesized thanks to sharp-edged corners and large enough size of seeds (Figure S9d).

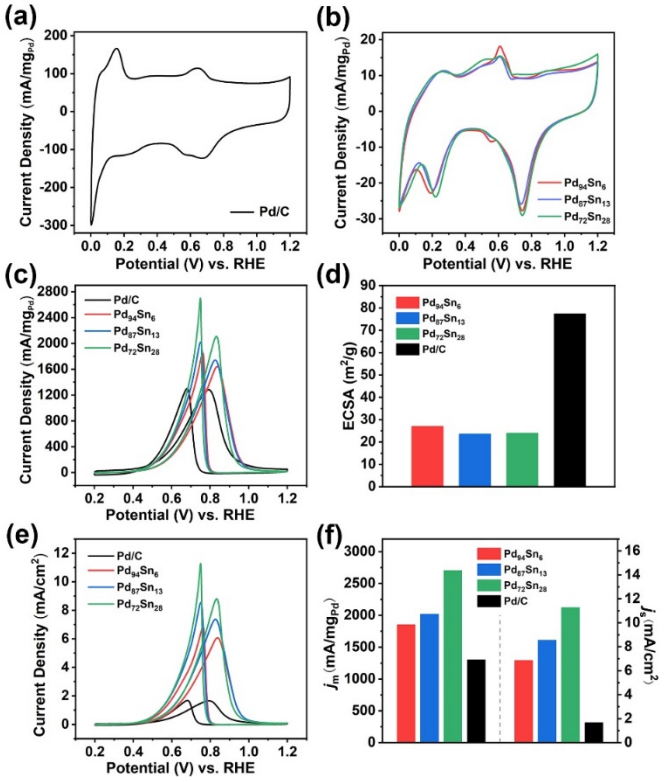

Figure 5. Electrochemical measurements of PdSn alloy catalysts towards EOR. (a, b) CV curves of commercial Pd/C (a) and PdSn alloys (b) conducted in 1 M KOH solution normalized to the mass of Pd. (c, e) CV curves of all the catalysts conducted in 1 M KOH solution containing 1 M ethanol normalized to the mass of Pd (c) and the ECSAs (e). (d) ECSAs of all the catalysts. (f) Mass and specific activities of all the catalysts.

PdSn octopods with different compositions were evaluated as electrocatalysts towards EOR. Firstly, X-ray photoelectron spectroscopy (XPS) was used to determine the valences states of Pd elements in PdSn octopods, and spectra of Pd 3d are shown in Figure S10. All the Pd 3d peaks can be deconvoluted into two peaks, suggesting the co-existence of metal and oxidation states. The peaks of Pd^0 $3d_{5/2}$ and $3d_{3/2}$ shifted to higher energy with respect to standard Pd^0, indicating the loss of electrons in Pd atoms. $Pd_{94}Sn_6$, $Pd_{87}Sn_{13}$, and $Pd_{72}Sn_{28}$ octopods were loaded uniformly onto the Vulcan XC-72R carbon black support as shown in Figure S11a-c, and the commercial Pd/C was chosen as a contrast sample (Figure S11d). The cyclic voltammetry (CV) tests of these four catalysts were conducted at room temperature in Ar-saturated 1 M KOH solutions at a sweep rate of 50 mV s^{-1} between 0 and 1.2 V vs. reversible

hydrogen electrode (RHE). Figure 5a and Figure 5b show the CV curves of Pd/C and three carbon-loaded PdSn nanocrystal catalysts normalized to the mass of Pd, respectively. The pronounced peaks at the negative sweep between 0.9 and 0.5 V in four CV curves are corresponding to the reduction of Pd (II) oxide.[44-46] The EOR activity of all the catalysts were evaluated by CV tests conducted at room temperature in Ar-saturated solution containing 1 M KOH and 1 M ethanol at a sweep rate of 50 mV s^{-1} between 0.2 and 1.2 V vs. RHE. Since the EOR activity of PdSn alloys was mostly contributed by Pd atoms, we normalized the current of CV curves above with respect to the mass of Pd,[23,47] as shown in Figure 5c. Among the four catalysts, carbon-loaded $Pd_{72}Sn_{28}$ exhibits the highest mass current density (2701 mA mg^{-1}), which is prominently higher than $Pd_{87}Sn_{13}$ (2019 mA mg^{-1}), $Pd_{94}Sn_6$ (1852 mA mg^{-1}), and 2.1 times higher than commercial Pd/C (1300 mA mg^{-1}). To measure the electrochemical specific area (ECSA) of each catalyst, we conducted CO-stripping tests (Figure S12) and calculated the charge transfer in the oxidation of monolayer CO adsorbed on the surface of nanocrystals. The ECSAs of four catalysts are shown in Figure 5d. The ECSA of commercial Pd/C is 77.4 $m^2 g^{-1}_{Pd}$, which is prominently higher than that of three PdSn alloys (27.0 $m^2 g^{-1}_{Pd}$ for $Pd_{94}Sn_6$, 23.6 $m^2 g^{-1}_{Pd}$ for $Pd_{87}Sn_{13}$, and 24.0 $m^2 g^{-1}_{Pd}$ for $Pd_{72}Sn_{28}$), probably due to the smaller size of Pd nanoparticles loaded on Pd/C. Subsequently, we normalized the CV curves of four catalysts for EOR by ECSAs to measure the intrinsic activities (i.e., specific activities), as shown in Figure 5e. $Pd_{72}Sn_{28}$ still exhibited the highest specific current density (11.27 mA cm^{-2}) and was superior to that of $Pd_{87}Sn_{13}$ (8.54 mA cm^{-2}), $Pd_{94}Sn_6$ (6.85 mA cm^{-2}), and 6.7 times higher than Pd/C (1.68 mA cm^{-2}). The histogram in Figure 5f shows the values of mass and specific activities of four catalysts. The cycling stabilities of all the catalysts were assessed by continuously running CV cycles between 0.2 and 1.2 V vs. RHE for 500 more cycles, and the mass activities were recorded against the cycle numbers in Figure S13. The mass activities of PdSn alloys are superior to that of commercial Pd/C, the current density of the latter one declined to virtually zero after 500 cycles. $Pd_{94}Sn_6$ exhibited the best stability with only 35.9% mass activity loss during cycling, that is, current density of 1187 mA mg^{-1} retained after 500 cycles, higher than that of $Pd_{87}Sn_{13}$ (1071 mA mg^{-1}) and $Pd_{72}Sn_{28}$ (957 mA mg^{-1}). TEM images of the catalysts after electrochemical stability test are shown in Figure S14, from which PdSn octopods show morphologies change including getting round at the corners to some extent and a little aggregation (Figure S14a-c). The commercial Pd/C exhibited severe agglomeration after cycling with respect to PdSn alloys (Figure S14d), which may be due to the high surface energy of Pd nanoparticles in small size. The decline rate of activities of PdSn alloys before 100 cycles was slower than after 100 cycles, which is the result of the combination of surface cleaning by CV process and the aggregation of nanocrystals as well as morphologies change.

To uncover the composition effect of PdSn alloys towards EOR, we conducted DFT calculations. Since the oxidation of adsorbed *CH_3CO by *OH is the rate determining step of EOR for Pd-based catalysts,[5,6] we investigated the adsorption strength of *CH_3CO on the surface of the Pd-based catalysts. Three models of (100)-terminated surfaces of ideal Pd, $Pd_{94}Sn_6$, and $Pd_{72}Sn_{28}$ were built, and we calculated the projected density of states (PDOS) of the Pd 4d-states, as shown in Figure 6a. The d-band center of $Pd_{72}Sn_{28}$ is -2.59 eV, which is prominently lower than that of $Pd_{94}Sn_6$ (-1.92 eV) and ideal Pd (-1.77 eV). Since the incorporation of Sn atoms will bring strong d-p orbital hybridization of Pd and Sn, thereby lowering the d-band center of Pd 4d-states.[23] From the previous work of Nørskov et al.,[48] the higher the d-band center with respect to the Fermi level, the higher the antibonding state energy, and the stronger the adsorption bonding of intermediates on the surface. As such, $Pd_{72}Sn_{28}$ should have the weakest adsorption strength. To demonstrate this conclusion, we placed a *CH_3CO on the (100) surface of each model as shown in Figure S15, and subsequently calculated the adsorption energies. From Figure 6b, the adsorption energy of *CH_3CO on $Pd_{72}Sn_{28}$ is -2.00 eV, which is higher than that of $Pd_{94}Sn_6$ (-2.55 eV) and ideal Pd (-2.65 eV), illustrating the weakest adsorption on the surface of $Pd_{72}Sn_{28}$, in accordance with the d-band theory. The weaker *CH_3CO adsorbed on the surface of catalysts, more active it will be, and thus easier it will be oxidized by *OH. Hence the catalytic activity of three catalysts follows a sequence of $Pd_{72}Sn_{28}$ (100) > $Pd_{94}Sn_6$ (100) > ideal Pd (100), which could be further supported by electrochemical analysis. From CO-stripping curves of three PdSn catalysts in Figure S12b, the oxidation peaks of mono-layer CO could be clearly observed. With the increase of Sn composition in PdSn catalysts, the peak position moves to low potential, suggesting the easier oxidation of CO molecules. This result demonstrates the weaker adsorption of CO on the surface of the nanocrystals. According to scaling relations described by Nørskov et al.,[49] the adsorption energies of adsorbates binding to the surface through carbon can be correlated and have a linear relation with the adsorption energy of CO. Therefore, the weaker adsorption of CO, the weaker adsorption of CH_3CO on the surface of PdSn alloys, which further demonstrates the best activity of $Pd_{72}Sn_{28}$ alloy octopods towards EOR.

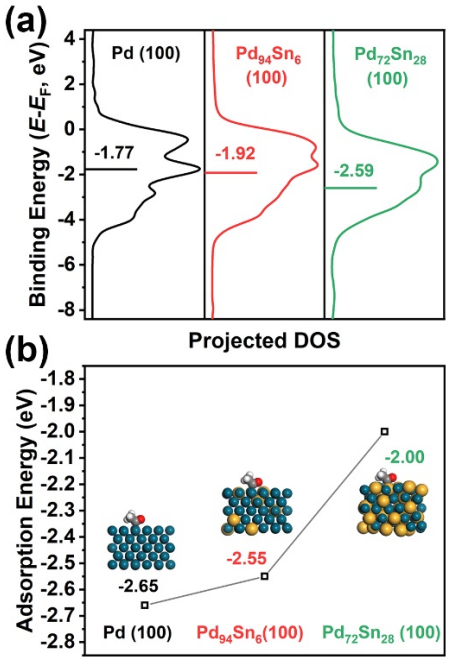

Figure 6. DFT calculations of the surfaces of Pd (100), $Pd_{94}Sn_6$ (100), and $Pd_{72}Sn_{28}$ (100). (a) PDOS of the Pd 4d-states. The positions of d-band center are marked by horizontal lines. (b) Adsorption energies of *CH_3CO.

Conclusions

In summary, we have demonstrated a facile seed-mediated approach to the synthesis of PdSn alloy octopods with tunable composition through Stranski-Krastanov growth mechanism. Firstly, Sn atoms deposited and diffused into the lattice of Pd with the retainment of the morphology of cube. Then, Sn atoms deposited preferentially

onto the eight corners of cubes due to the increased reduction rate, and inter-diffused with Pd atoms moved from {100} facets, leading to the formation of PdSn alloy octopods. Such nanocrystals exhibited remarkably enhanced mass and specific activity and stability towards EOR with respect to commercial Pd/C. Among them, $Pd_{72}Sn_{28}$ octopods showed the highest mass and specific activity (2701 mA mg^{-1} and 11.27 mA cm^{-2}), which are 2.1 and 6.7 times higher than those of commercial Pd/C. DFT calculations revealed that the lowest d-band center of the (100) surface of $Pd_{72}Sn_{28}$ weakens the adsorption of the key intermediate $*CH_3CO$, bringing the best catalytic activity for EOR. Our work not only provides a facile and general approach to the synthesis of nanocrystals with precisely controlled branches and compositions, but also offers a great opportunity to design efficient catalysts for EOR and beyond.

Conflicts of interest

The authors declare that they have no conflict of interest.

Acknowledgements

The work on electron microscopy was carried out in the Center for Electron Microscopy of Zhejiang University. This work was supported by the National Science Foundation of China (51871200), National Program for Support of Top-notch Young Professionals, National Key R&D Program of China (2018YFB2200102), and Foundation for Innovative Research Groups of the National Natural Science Foundation of China (61721005).

Notes and references

1 M. Z. F. Kamarudin, S. K. Kamarudin, M. S. Masdar and W. R. W. Daud, *Int. J. Hydrogen Energy*, 2013, **38**, 9438-9453.
2 J. Wang, Z. Pei, J. Liu, M. Hu, Y. Feng, P. Wang, H. Wang, N. Nie, Y. Wang, C. Zhi and Y. Huang, *Nano Energy*, 2019, **65**, 104052.
3 M. A. F. Akhairi and S. K. Kamarudin, *Int. J. Hydrogen Energy*, 2016, **41**, 4214-4228.
4 J. Bai, D. Liu, J. Yang and Y. Chen, *ChemSusChem*, 2019, **12**, 2117-2132.
5 Z. X. Liang, T. S. Zhao, J. B. Xu and L. D. Zhu, *Electrochim. Acta*, 2009, **54**, 2203-2208.
6 C. Bianchini and P. Shen, *Chem. Rev.*, 2009, **109**, 4183-4206.
7 E. Antolini, *Energy Environ. Sci.*, 2009, **2**, 915-931.
8 C. Liu, Y. Shen, J. Zhang, G. Li, X. Zheng, X. Han, L. Xu, S. Zhu, Y. Chen, Y. Deng and W. Hu, *Adv. Energy Mater.*, 2022, 2103505.
9 H. Yang, X. Zhang, H. Zou, Z. Yu, S. Li, J. Sun, S. Chen, J. Jin and J. Ma, *ACS Sustainable Chem. Eng.*, 2018, **6**, 7918-7923.
10 M. Wang, D. Li, Y. Tian, J. Zhao, Z. Yue, X. Wang, X. Ma, J. Wang, T. Hu, J. Jia and H. Wu, *ACS Appl. Mater. Interfaces*, 2021, **13**, 53777-53786.
11 W. Wang, X. Zhang, Y. Zhang, X. Chen, J. Ye, J. Chen, Z. Lyu, X. Chen, Q. Kuang, S. Xie and Z. Xie, *Nano Lett.*, 2020, **20**, 5458-5464.
12 T. Wu, M. Sun and B. Huang, *InfoMat.*, 2020, **2**, 715-734.
13 Z. Lyu, X. G. Zhang, Y. Wang, K. Liu, C. Qiu, X. Liao, W. Yang, Z. Xie and S. Xie, *Angew. Chem. Int. Ed.*, 2021, **60**, 16093-16100.
14 L. Ma, H. He, A. Hsu and R. Chen, *J. Power Sources*, 2013, **241**, 696-702.
15 H. Xu, P. Song, Y. Zhang and Y. Du, *Nanoscale*, 2018, **10**, 12605-12611.
16 J. Huang, Q. Liu, Y. Yan, N. Qian, X. Wu, L. Ji, X. Li, J. Li, D. Yang and H. Zhang, *Nanoscale Adv.*, 2022, **4**, 111-116.
17 M. Liu, M. Xie, Y. Jiang, Z. Liu, Y. Lu, S. Zhang, Z. Zhang, X. Wang, K. Liu, Q. Zhang, T. Cheng and C. Gao, *J. Mater. Chem. A*, 2021, **9**, 15373-15380.
18 K. Jiang, P. Wang, S. Guo, X. Zhang, X. Shen, G. Lu, D. Su and X. Huang, *Angew. Chem. Int. Ed.*, 2016, **55**, 9030-9035.
19 A. S. Douk, H. Saravani and M. Noroozifar, *Int. J. Hydrogen Energy*, 2017, **42**, 15149-15159.
20 H. Wang, L. Jiao, L. Zheng, Q. Fang, Y. Qin, X. Luo, X. Wei, L. Hu, W. Gu, J. Wen and C. Zhu, *Adv. Funct. Mater.*, 2021, **31**, 2103465.
21 X. Lao, M. Yang, X. Sheng, J. Sun, Y. Wang, D. Zheng, M. Pang, A. Fu, H. Li and P. Guo, *ACS Appl. Energy Mater.*, 2022, **5**, 1282-1290.
22 W. Du, K. E. Mackenzie, D. F. Milano, N. A. Deskins, D. Su and X. Teng, *ACS Catal.*, 2012, **2**, 287-297.
23 Q. Gao, T. Mou, S. Liu, G. Johnson, X. Han, Z. Yan, M. Ji, Q. He, S. Zhang, H. Xin and H. Zhu, *J. Mater. Chem. A*, 2020, **8**, 20931-20938.
24 N. Ma, S. Wang, X. Liu, Y. Sun, Y. Yin, L. Y. Zhang and P. Guo, *Sci. China Mater.*, 2020, **63**, 2040-2049.
25 B. Lim and Y. Xia, *Angew. Chem. Int. Ed.*, 2011, **50**, 76-85.
26 A. R. Poerwoprajitno, L. Gloag, T. M. Benedetti, S. Cheong, J. Watt, D. L. Huber, J. J. Gooding and R. D. Tilley, *Small*, 2019, **15**, 1804577.
27 M. Luo, Y. Qin, M. Li, Y. Sun, C. Li, Y. Li, Y. Yang, F. Lv, D. Wu, P. Zhou and S. Guo, *Sci. Bull.*, 2020, **65**, 97-104.
28 S. Xue, W. Deng, F. Yang, J. Yang, I. S. Amiinu, D. He, H. Tang and S. Mu, *ACS Catal.*, 2018, **8**, 7578-7584.
29 N. Gao, X. Wu, X. Li, J. Huang, D. Li, D. Yang and H. Zhang, *RSC Adv.*, 2020, **10**, 12689-12694.
30 S. G. Corcoran, G. S. Chakarova and K. Sieradzki, *Phys. Rev. Lett.*, 1993, **71**, 1585-1588.
31 A. Baskaran and P. Smereka, *J. Appl. Phys.*, 2012, **111**, 044321.
32 J. Liang and Z. Suo, *Appl. Phys. Lett.*, 2001, **79**, 3251-3253.
33 A. Bellec, Y. Garreau, J. Creuze, A. Vlad, F. Picca, M. S. Simkin and A. Coati, *Phys. Rev. B*, 2017, **96**, 085414.
34 L. Tao, Z. Xia, Q. Zhang, Y. Sun, M. Li, K. Yin, L. Gu and S. Guo, *Sci. Bull.*, 2021, **66**, 44-51.
35 Y. Xiong, Y. Ma, J. Li, J. Huang, Y. Yan, H. Zhang, J. Wu and D. Yang, *Nanoscale*, 2017, **9**, 11077-11084.
36 M. Jin, H. Liu, H. Zhang, Z. Xie, J. Liu and Y. Xia, *Nano Res.*, 2011, **4**, 83-91.
37 J. Huang, Y. Yan, X. Li, X. Qiao, X. Wu, J. Li, R. Shen, D. Yang and H. Zhang, *Nano Res.*, 2020, **13**, 2641-2649.
38 X. Xia, S. Xie, M. Liu, H. C. Peng, N. Lu, J. Wang, M. J. Kim and Y. Xia, *Proc. Natl. Acad. Sci. U.S.A.*, 2013, **110**, 6669-6673.
39 M. Zhao, Z. Chen, Y. Shi, Z. D. Hood, Z. Lyu, M. Xie, M. Chi and Y. Xia, *J. Am. Chem. Soc.*, 2021, **143**, 6293-6302.
40 J. Wu, W. Gao, J. Wen, D. J. Miller, P. Lu, J. M. Zuo and H. Yang, *Nano Lett.*, 2015, **15**, 2711-2715.
41 Z. Yang, L. Shang, X. Xiong, R. Shi, G. I. N. Waterhouse and T. Zhang, *Chem. Eur. J.*, 2020, **26**, 4090-4096.
42 F. Li, Q. Shao, M. Hu, Y. Chen and X. Huang, *ACS Catal.*, 2018, **8**, 3418-3423.
43 V. K. LaMer and R. H. Dinegar, *J. Am. Chem. Soc.*, 1950, **72**, 4847-4854.
44 A. L. Wang, X. J. He, X. F. Lu, H. Xu, Y. X. Tong and G. R. Li, *Angew. Chem.*, 2015, **127**, 3740-3744.
45 W. Huang, X. Y. Ma, H. Wang, R. Feng, J. Zhou, P. N. Duchesne, P. Zhang, F. Chen, N. Han, F. Zhao, J. Zhou, W. B. Cai and Y. Li. *Adv. Mater.*, 2017, **29**, 1703057.
46 G. M. Alvarenga, I. B. C. Gallo and H. M. Villullas, *J. Catal.*, 2017, **348**, 1-8.
47 S. Mondal, V. S. K. Choutipalli, B. K. Jena, V. Subramanian and C. R. Raj, *J. Phys, Chem. C*, 2020, **124**, 9631-9643.
48 J. K. Nørskov, F. A. Pedersen, F. Studt and T. Bligaard, *Proc. Natl. Acad. Sci. U.S.A.*, 2011, **108**, 937-943.

49 A. A. Peterson and J. K. Nørskov, *J. Phys, Chem. Lett.*, 2012, **3**, 251-258.